ACS APPLIED MATERIALS & INTERFACES

www.acsami.org

Research Article

Bioinspired Separator with Ion-Selective Nanochannels for Lithium Metal Batteries

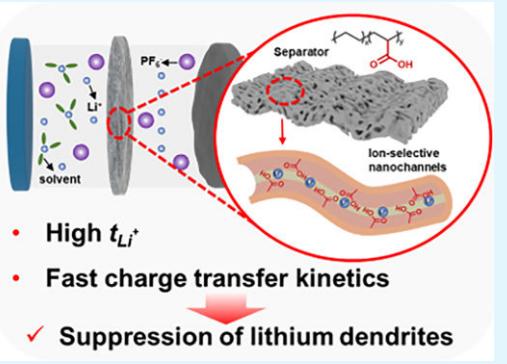
Yi Chen, Philip Mickel, Huijie Pei, Yingfeng Wen, Xin Guan, Yun Wang, Xuyang Wang, Omar Al Mhtachem, Cheng Zhang, Hui Nie,* Xingping Zhou, Petr Kral,* and Xiaolin Xie*

Cite This: *ACS Appl. Mater. Interfaces* 2023, 15, 18333−18342

Read Online

ACCESS | Metrics & More | Article Recommendations | Supporting Information

ABSTRACT: The free transport of anions through commercial polyolefin separators used in lithium metal batteries (LMBs) gives rise to concentration polarization and rapid growth of lithium dendrites, leading to poor performance and short circuits. Here, a new poly(ethylene-*co*-acrylic acid) (EAA) separator with functional active sites (i.e., carboxyl groups) distributing along the pore surface was fabricated, forming bioinspired ion-conducting nanochannels within the separator. As the carboxyl groups effectively desolvated Li^+ and immobilized anion, the as-prepared EAA separator selectively accelerated the transport of Li^+ with transference number of Li^+ (t_{Li^+}) up to 0.67, which was further confirmed by molecular dynamics simulations. The battery with the EAA separator can be stably cycled over 500 h at 5 mA cm^{-2}. The LMBs with the EAA separator have exceptional electrochemical performance of 107 mAh g^{-1} at 5 C and a capacity retention of 69% after 200 cycles. This work provides new commercializable separators toward dendrite-free LMBs.



KEYWORDS: *lithium anode, lithium metal battery, separator, poly(ethylene-co-acrylic acid), ion-selective nanochannels*

Downloaded via UNIV OF ILLINOIS CHICAGO on April 15, 2023 at 15:50:29 (UTC).
See https://pubs.acs.org/sharingguidelines for options on how to legitimately share published articles.

INTRODUCTION

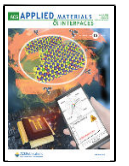
Lithium metal batteries (LMBs), using microporous polyolefin separators to isolate anodes and cathodes, are excellent energy storage devices for electric vehicles and powering portable electronic devices due to their high power density.[1−3]

The separators, which provide pathway for ion migration during the charging/discharging process, have a huge impact on the performance of LMBs.[4,5] Though the polyolefin separators are dimensionally stable, their hydrophobic nature affords high energy barriers for the entry and passage of ions.[6−8] In addition, with an inert polyolefin separator, the anions in the electrolyte solution move faster than solvated Li^+ ions, leading to low transference number of t_{Li^+} = 0.2−0.4.[9,10] Here, t_{Li^+} is defined as $\mu_{Li^+}/(\mu_{Li^+} + \mu_{anion})$, where μ_{Li^+} and μ_{anion} refer to the mobilities of Li^+ and anion, respectively.[11] According to the well-accepted nucleation mechanism of lithium dendrites proposed by Sand and co-workers, lithium dendrite deposition is closely related to t_{Li^+}, with a low t_{Li^+} leading to rapid growth of lithium dendrites, resulting in short circuiting and even explosion of LMBs.[12−14]

Currently, various inorganic nanoparticles and/or polymers have been coated on the surface of microporous polyolefin separators, or functional groups have been graft on porous membrane by radiation to improve their electrolyte wettability.[15−19] However, these strategies only modify their outer surface property and can not improve the inherent properties of inert pores within the polyolefin separator,[20,21] or such processes require additional equipment, increase the cost and may decrease the structural stability of the separator. Biological ion channels provide ion conducting pathways to facilitate ionic conduction across the hydrophobic bilayer lipid membrane with high selectivity (Figure 1a).[22,23] Functionality of ion channels is realized through a circular arrangement of proteins, which generates nanopores with a hydrophilic interior and flexible ion selectivity filters.[24] Inspired by biological ion channels with high ion permeability and selectivity, a strategy of introducing ion-conducting channels with polar "active sites" throughout the scaffold of polyolefin-based separator is proposed. The "active sites" in ion channels are expected to increase the polarity of the embedded surface of pores and provide interaction sites with ions, thus accelerating ion transport and increasing the t_{Li^+} of the battery.

Poly(ethylene-*co*-acrylic acid) (EAA) is a class of commercially available copolymer consisting of inert full-carbon backbone and polar side chain with carboxyl groups. In this work, a novel EAA separator with polar carboxyl groups alongside the pores' surface has been fabricated by a facile

Received: January 29, 2023
Accepted: March 16, 2023
Published: March 28, 2023



© 2023 American Chemical Society

https://doi.org/10.1021/acsami.3c01311
ACS Appl. Mater. Interfaces 2023, 15, 18333−18342

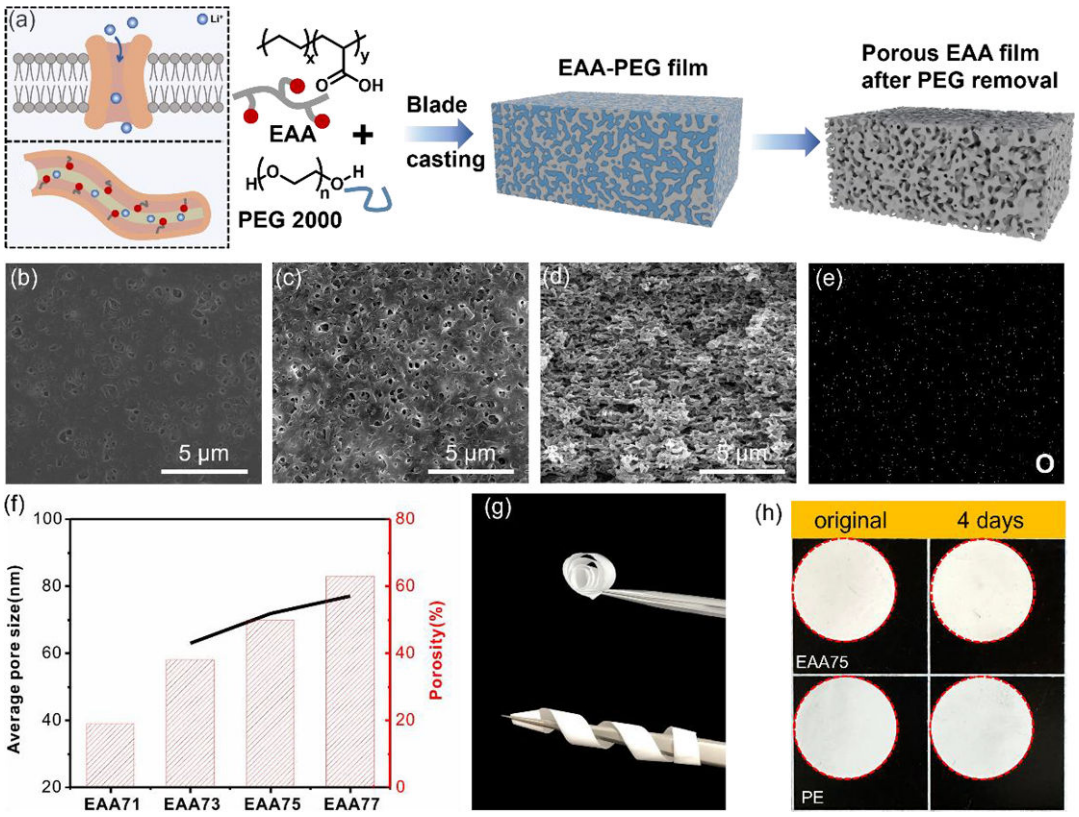


Figure 1. (a) Fabrication process of EAA separators. SEM images of (b) substrate-facing side and (c) air-facing side surfaces of EAA75 separator. (d) Cross-sectional SEM image of EAA75 and (e) the corresponding EDX mapping of O. (f) Porosity and average pore size of EAA separators prepared with different adding amount of PEG 2000. (g) Photographs of EAA75 separators under different bending conditions. (h) Photographs of PE and EAA75 separators before and after drying−rewetting−drying process.

template-leaching method. The as-prepared EAA separator possesses good dimensional stability similar to commercial polyolefin separator, which can stand against swelling by polar electrolytes. Meanwhile, the ion channels with carboxyl groups on the pores' surface not only enhance wettability but also immobilize anion through hydrogen bonding and accelerate Li^+ transport by desolvation effect, boosting t_{Li^+} to 0.67. The kinetic of ion transport within EAA separator was further confirmed by molecular dynamics simulations. With increased t_{Li^+}, stable Li plating/stripping and homogeneous solid electrolyte interface (SEI) layer can be achieved by accelerating the charge-transfer kinetics on the Li anode. Batteries assembled with EAA separators can be stably cycled for over 500 h under a current density of 5 mA cm^{-2}. The cells containing the EAA separator have an exceptional electrochemical performance of 107 mAh g^{-1} at 5 C and a capacity retention of 69% after 200 cycles. Our research suggests that this novel EAA separator with polar carboxyl groups placed along the surface of its pores has great potential to serve as a high-performance separator for LMBs.

RESULT AND DISCUSSION

Fabrication of EAA Separators. The preparation of EAA separators using the template-leaching method with polyethylene glycol (PEG) 2000 as the template is illustrated in Figure 1a. While the skeleton of EAA is polyethylene, few solvents can dissolve it at room temperature. After screening various solvents and dissolution conditions, such as decahydronaphthalene, toluene, and tetrahydrofuran (THF), THF was chosen due to its good solubility toward both EAA and PEG 2000 at 65 °C. Thus, a homogeneous film can be prepared from EAA/PEG2000 blend by solution-casting. After the film has been prepared and left standing at 60 °C for 1 min, PEG 2000 was removed by immersing in ethanol bath to form a porous structure within EAA. There are two advantages for PEG 2000 as the pore generator agent. First, the viscosity of the casting solution was increased with the addition of PEG 2000, which is beneficial for the formation of uniform film during the solution-casting process. Second, the stronger association of carboxyl group with PEG 2000 than that of the nonpolar polyethylene backbone is beneficial to the formation of nanoporous separators enriched with a −COOH group along the pore walls after the removal of PEG 2000. Here, a series of porous separators with different amounts of pore generator PEG 2000 were fabricated. The as-prepared separators are named as EAA71, EAA73, EAA75, and EAA77, meaning the weight ratios of EAA and PEG 2000 in casting solution are 7:1, 7:3, 7:5, and 7:7, respectively (Figure S1). First, detailed characterizations of the nanoporous separators (EAA75 was chosen as typical example) were carried out using scanning electron microscopy (SEM). As represented in Figure 1b,c, the surface morphologies of the EAA75 separators on the air- and substrate-facing sides are different. The substrate-facing sides of the separator have fewer pores, while the air-facing sides represent a rougher morphology. Although the surface morphologies of the two sides of the separators are different, their sizes of pores are all within the nanometer range and well-distributed on the surface. To observe the overall film uniformity and pore-size distribution inside the film, the cross-sectional morphology of

https://doi.org/10.1021/acsami.3c01311
ACS Appl. Mater. Interfaces 2023, 15, 18333−18342

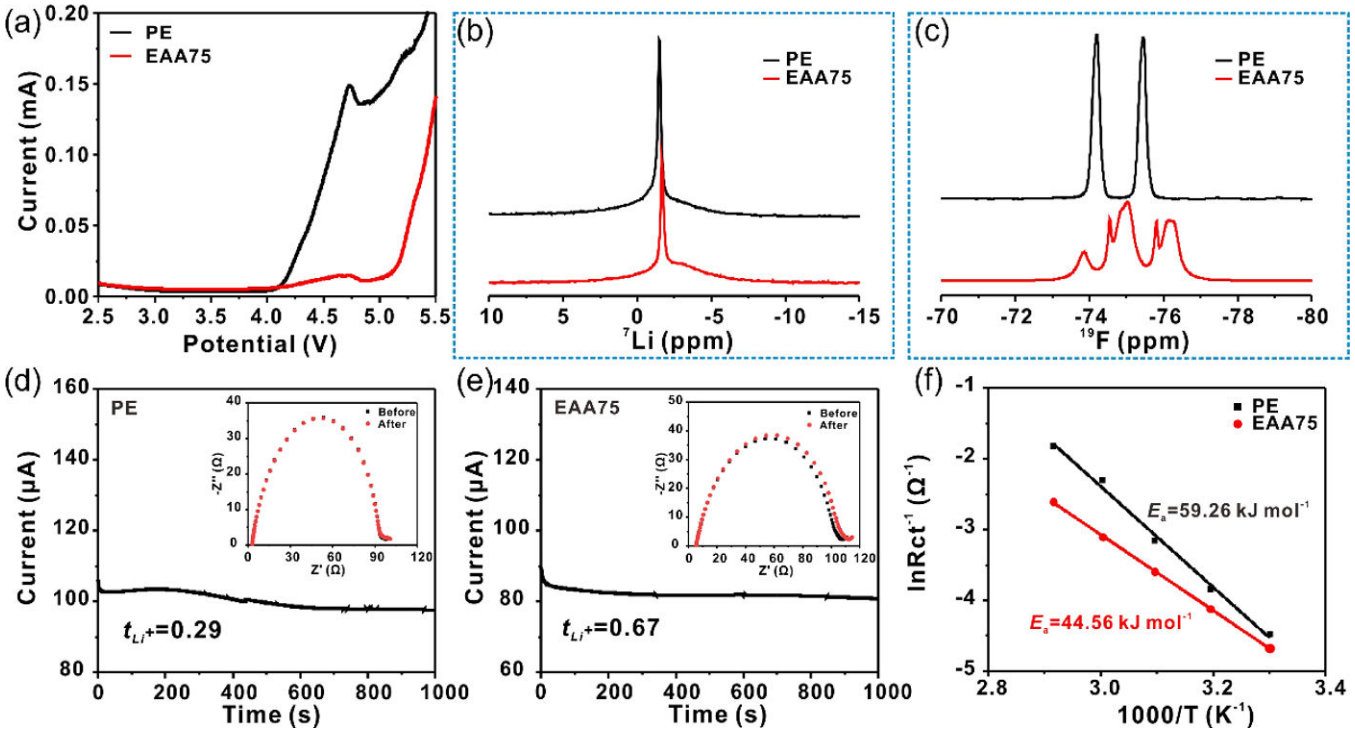


Figure 2. (a) LSV curves of Li/separator/stainless steel cells with different separators. Solid-state ^{7}Li NMR (b) and ^{19}F NMR (c) spectra of PE and EAA75 separators. Chronoamperometry profiles of PE separator (d) and EAA75 separator (e). Inset are the AC impedance spectra before and after polarization. (f) Calculation of activation energy (E_a) from Nyquist plots.

EAA75 was investigated. As shown in Figure 1d, the EAA separator possessed a highly connected and uniformly distributed pore structure, ensuring the migration of Li^+. Meanwhile, energy-dispersive X-ray (EDX) mapping confirmed that the carboxyl group is evenly distributed alongside the EAA separator (Figure 2e). Further, the influence of adding amount of pore generator PEG 2000 on the porosity and pore size of the nanoporous separators was investigated by gas permeation method. As shown in Figures 1f and S2, the porosity of EAA separators was continuously increased with the increase amount of PEG 2000 (Table S1). The average pore size became larger with more PEG 2000, indicating the majority of pores are created by leaching of the PEG 2000, and the dimension of the PEG 2000 clusters in the casting films increased with the quantity of PEG 2000. As displayed in Figure S3, the ionic conductivity of various EAA separators increased with porosity. However, the strength decreased with increased porosity. To balance the electrochemical performance and strength, EAA75 separator was chosen for the following studies. As illustrated in Figure 1g, EAA75 is an opaque film as the result of light scattering by nanopores, and it is flexible enough to maintain its original shape after curling. It is worth noting that the as-prepared EAA75 separator possesses high dimensional stability. For some porous separators fabricated by either a dry or wet process, pore collapse occurs due to capillary forces acting on the pore surface during the drying−rewetting−drying process, which is a drawback for their application and storage.[25−27] Impressively, the EAA75 separators retain their opacity due to remaining pores after the drying−rewetting−drying process (Figure 1h). The preserved porous structure was further confirmed by SEM images (Figure S4). Furthermore, the pore size distribution of EAA75 after drying−rewetting−drying process was also measured, and it is in the same range as that of the original EAA75 (Figure S5), which demonstrates the structure stability of EAA75. It is supposed that the inert polyethylene skeleton has low affinity with the solvents and thus efficiently reduces the strength of capillary forces. This property is beneficial for further surface modification of the EAA75 porous separator. The above results clearly suggest the capability of the as-developed template leaching method for the fabrication of uniform EAA separators with high dimensional stability.

Characterizations of EAA75 Separator. Due to the polar carboxyl groups of EAA75, the as-obtained separator yields improved electrolyte wettability. Figure S6 shows the contact angles of liquid electrolyte on EAA75 and commercial PE separators. As expected, the contact angles of both sides (41.0° and 40.3°) of EAA75 porous separator were lower than PE (44.7°), illustrating a better wettability of EAA75 to the liquid electrolyte. Owing to the better wettability, larger pore size, and higher porosity, the electrolyte uptake of EAA75 is 173%, higher than that of PE (Table S2). Additionally, the linear sweep voltammetry (LSV) curves shows that PE and EAA75 can stably operate at a voltage of U = 2.5−3.9 V, showing the electrochemical stability of both separators (Figure 2a). As shown in Figure S7, thanks to improved wettability, the ion conductivity of EAA75 reaches 0.49 mS cm^{-1}, higher than that of PE (0.33 mS cm^{-1}), providing a better electrochemical performance.

The carboxyl groups not only endow EAA separator with good electrolyte wettability and high electrolyte uptake but also provide "active sites" to interact with cations and anions in the electrolyte. Solid-state NMR measurements were carried out to investigate the interaction between EAA75 separator and electrolyte. Here, PE separator was used as a blank comparison. For sample preparation, PE and EAA75 porous

https://doi.org/10.1021/acsami.3c01311
ACS Appl. Mater. Interfaces 2023, 15, 18333−18342

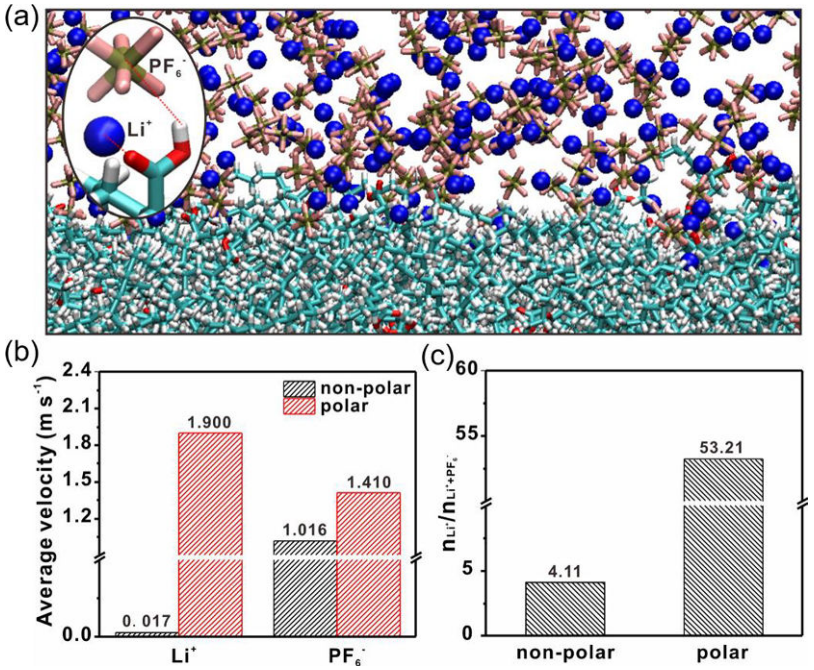


Figure 3. (a) Atomistic molecular dynamics simulations of Li^+ (blue spheres) and PF_6^- ions (pink and gold knucklebones) with EAA polymer separator (teal and red). Inset: Interaction of ions with carboxyl group on EAA separator. (b) Average velocity of Li^+ ions and PF_6^- ions migrated on the surface of the nonpolar and polar separators with an external electric field. (c) Calculated ratio between average transmission numbers of Li^+ ions and PF_6^- ions on the surface of the nonpolar and polar separators with an external electric field.

separators were first soaked in liquid electrolytes for 10 min. $LiPF_6$ salt was adsorbed onto the separators after removing the solvents. The resulting films were further dried and subjected to measurements. As shown in Figure 2b, there is one sharp peak (−1.8 ppm) and one broad peak (−3.0 ppm) in the ^7Li NMR spectrum of EAA75, which is distinct from the PE sample (−1.5 ppm). It is suggested that the peak at −1.8 ppm represents Li^+ around polyolefin backbone, like that of PE porous separator. The front-field-shifted peak at −3.0 ppm represents Li^+ near the carboxyl group, suggesting the EAA75 separator had a strong interaction with Li^+. The above result suggests that the carboxyl groups on the pore surface act as active sites for the transport of Li ions. Similarly, ^{19}F NMR further indicates the interaction between −COOH and PF_6^- in Figure 2c. It can be seen that there are two peaks (−74.2 ppm and −75.4 ppm) in the ^{19}F NMR spectrum of PE, from PF_6^-. Interestingly, peaks with different chemical shifts of −73.8 ppm, −74.5 ppm, −75.0 ppm, −75.8 ppm, and −76.1 ppm were observed for EAA75 sample, suggesting the −COOH units provide different environments for PF_6^-. It is supposed that the −COOH units form hydrogen bonding and act as anchor for PF_6^-.[28]

Effects of EAA75 Separator on Suppressing the Growth of Lithium Dendrite. The EAA75 separator can not only delay the dendrite nucleation by increasing the t_{Li^+} but also benefit stable Li plating/stripping by accelerating the charge-transfer kinetics, lowering nucleation overpotential, and decreasing the internal resistance. According to the Sand's time (t_{Sand}), the onset of dendrite nucleation of EAA75 separator can be delayed with increased t_{Li^+}. The t_{Li^+} of PE and EAA75 was estimated through chronoamperometry and electrochemical impedance spectroscopy (EIS) analysis to be 0.29 and 0.67, respectively, as shown in Figure 2(d,e). The higher t_{Li^+} of EAA75 is mainly due to the carboxyl groups alongside the pore surface of the separator. While the carboxyl groups have unshared electron pairs, it is helpful to the desolvation of Li^+ and increase the mobility of Li^+ in battery. Here, temperature-dependent EIS measurements were carried out to investigate the Li^+ desolvation of EAA75 separator (Figure S8). The activation energy (E_a) of ion desolvation can be obtained by the linear fitting $\ln(R_{ct}^{-1})$ vs $1/T$ according to Arrhenius formula:[29]

$$1/R_{ct} = A \exp(-E_a/RT) \quad (1)$$

As shown in Figure 2f, the activation energy of EAA75 separator is 44.56 kJ mol^{-1}, lower than that of PE separator (E_a = 59.26 kJ mol^{-1}). The lower E_a of EAA75 separator means the faster Li^+ migration and the carboxyl groups are beneficial to the desolvation of Li^+, resulting the faster ion transfer kinetics.[29−31] Furthermore, the hydrogen bonding between PF_6^- and −COOH decreases the concentration polarization through anchoring the PF_6^- to alleviate the concentration polarization.

To further understand the observations, we modeled the experimental systems by classical molecular dynamics simulations,[32,33] as displayed in Figure 3. Two systems were simulated and compared with the experiments. Both systems were formed by a flat EAA separator (132 nm^2) consisting of an identical 23:1 ethylene to acrylic acid monomer molar ratio, covered by liquid electrolyte. In the liquid electrolyte, there are 6,000 ethylene carbonate and 3,380 diethyl carbonate molecules (1:1 volume ratio). The liquid electrolyte also had 830 Li^+ and PF_6^- ion pairs (1 M concentration of $LiPF_6$). The compositions of the modeled systems matched the conditions in the real EAA separator. In one system, we used the correct partial charges of the (overall neutral) carboxyl groups to model the separator surface (polar system). In the other system, all partial charges of carboxyl groups in the separator were set to zero to mimic a free solvent with no coupling to the separator (the nonpolar system).

https://doi.org/10.1021/acsami.3c01311
ACS Appl. Mater. Interfaces 2023, 15, 18333−18342

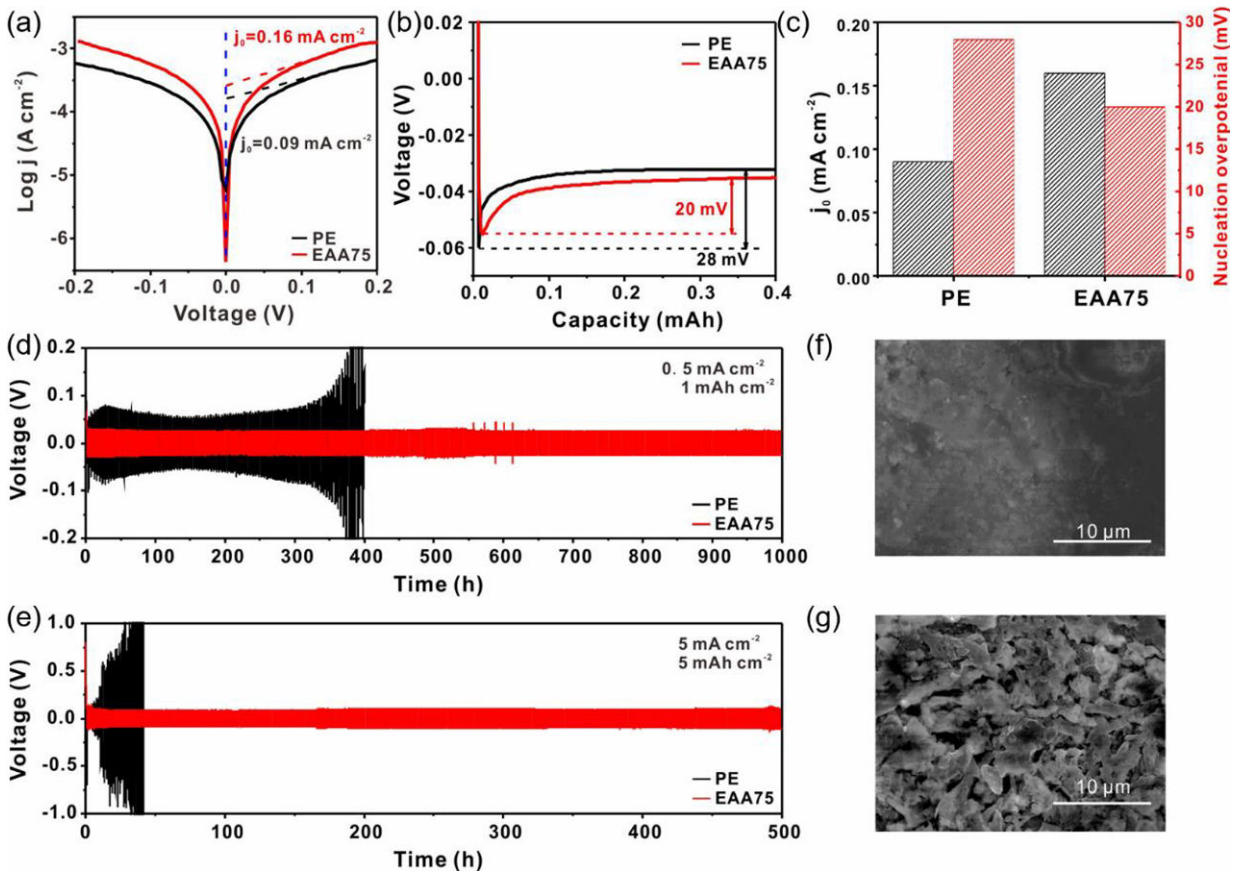


Figure 4. (a) Tafel plots of the Li symmetric cells with PE and EAA75 separators. (b) Voltage profiles of Cu||Li cells with PE and EAA75 separators at 0.5 mA cm^{-2} for 1.0 mAh cm^{-2}. (c) Summary of exchange current density and nucleation overpotentials. Galvanostatic test of Li||Li symmetric cells with PE and EAA75 separators at 0.5 mA cm^{-2} (d) and 5 mA cm^{-2} (e). SEM images of Li electrodes with EAA75 (f) and PE (g) after cycling for 100 h at 0.5 mA cm^{-2} for 1.0 mAh cm^{-2}.

Both systems were simulated for over 100 ns in an electric field of E = 1.3 MV/m. The particle-mesh Ewald (PME) method was used to evaluate the long-range Coulombic interactions. As compared in Figure 3b,c, in the nonpolar system, PF_6^- ions had an average velocity of $v_{PF_6^-}$ = 1.016 m/s, while Li^+ ions had an average velocity v_{Li^+} = 0.017 m/s. Therefore, PF_6^- ions were moving and mostly responsible for a total electric current of $I = 4.6 \times 10^{-7}$ A, while the Li^+ ions were practically static (pulled in opposite direction than PF_6^-). In the polar system, PF_6^- ions had an average velocity of $v_{PF_6^-}$ = 1.41 m/s, and Li^+ ions had an average velocity of v_{Li^+} = 1.90 m/s. Therefore, Li^+ ions were moving much faster pulling PF_6^- ions, which were probably affected more by the presence of the separator. Here, Li^+ ions were predominantly responsible for the total electric current of $I = 0.56 \times 10^{-7}$ A. Therefore, we show that Li^+ ions are more mobile in EAA75, resulting in a larger transference number. As the formation of dendrites is directly related to a small Li^+ transference number,[12−14] these separators can cause a reduced dendrite formation during battery cycling. With the synergistic effect of desolvation and hydrogen bonding, t_{Li^+} can increases significantly in EAA75, which can lead to excellent performance of these separators in dendrite inhibition.

Overall, we expect that EAA75 separator can cause fast metallic Li nucleation and uniform plating/stripping by accelerating the charge-transfer kinetics, lowering nucleation overpotential and decreasing the internal resistance. The exchange current density (j_0) is a key parameter reflecting the kinetics of the electrochemical reactions on the separator/anode interface, especially the charge-transfer kinetics of solid electrolyte interphase (SEI).[34−37] Here, j_0 is calculated from the linear fit of the Tafel plot (eq 2) at a voltage range of U = 115−175 mV, which is extracted from the measured cyclic voltammetry (CV) curves using the Li||Li cells (Figure 4a)

$$\eta = a + b \log(j) \tag{2}$$

where η is the overpotential, j is the current density, and a and b are constants.

In EAA75, j_0 = 0.16 mA cm^{-2}, almost two times higher than that of PE (0.09 mA cm^{-2}). Higher j_0 means faster electrochemical kinetics, suggesting the carboxyl groups of EAA75 separator lower the charge transfer barrier between Li anode and separator. The EIS spectra further confirm the faster kinetics of SEI. As shown in Figure S9, the EAA75 based battery had a lower impedance of 75 Ω than PE (80 Ω). The impedance of EAA75 increased to 200 Ω, while that of PE increased to 270 Ω after 100 cycles at 1 C. The above results indicate that cells assembled with EAA75 own a much more uniform SEI after cycling and stable lithium deposition behavior, which accounts for the lower impendence. Additionally, according to the Butler−Volmer equation (eq 3), the exchange current density can be viewed as a kind of idle current for charge exchange across the interface, meaning the lower j_0, the more sluggish the kinetics, and hence the larger the overpotential.[38,39] In other words, the battery with a higher

https://doi.org/10.1021/acsami.3c01311
ACS Appl. Mater. Interfaces 2023, 15, 18333−18342

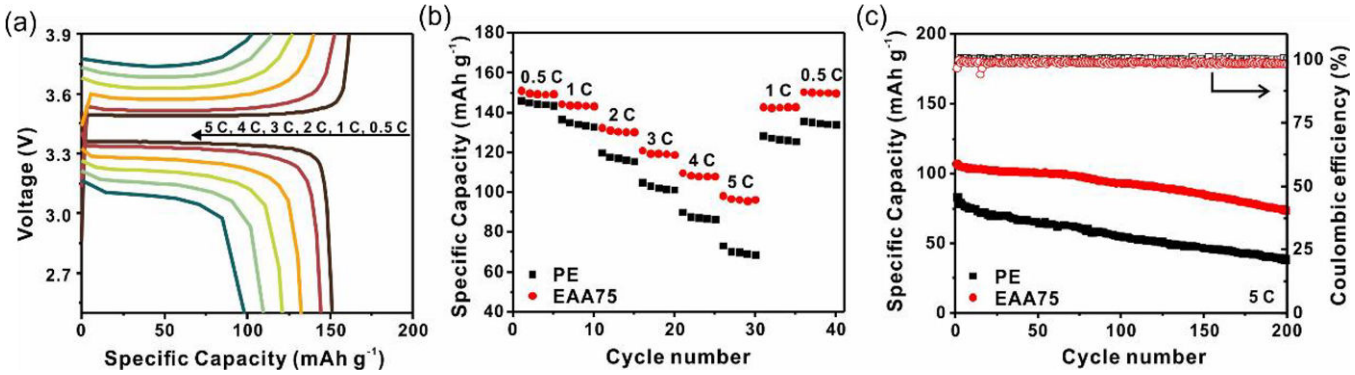


Figure 5. (a) Charge−discharge profiles of EAA75 assembled cells at different current densities. (b) Rate capability of LFP|PE|Li and LFP|EAA75|Li cells. (c) Long-term cycling tests of LFP|PE|Li and LFP|EAA75|Li cells at 5 C.

j_0 has faster lithium ion kinetics and the overpotential for lithium ion deposition can be lowered, resulting in more uniform lithium deposition

$$j = j_0[e^{-\alpha f\eta} - e^{(1-\alpha)f\eta}] \quad (3)$$

where j is the current density, j_0 is the exchange current density, η is the overpotential, and α and f are constant.

While j_0 reflects the overpotential on the anode, Cu||Li cells with PE and EAA75 separators were assembled to further evaluate their nucleation overpotential and Li plating/stripping performance. The nucleation process of metallic Li on Cu foil was studied with the voltage profiles of Cu|PE|Li and Cu|EAA75|Li cells, and the nucleation overpotential is determined by the voltage difference between the lowest transient potential and the stable cycling potential. A higher overpotential leads to a larger nucleation energy barrier for metallic Li deposition, and this is one of the critical reasons for the growth of dendritic Li during plating.[40,41] As shown in Figure 4b,c, first, a sharp voltage drop to −55 mV was observed for Cu|EAA75|Li cell at discharge rate of 0.5 mA cm^{-2}, which corresponds to the metallic Li nucleation process on Cu foil. Then, the voltage gradually rises and becomes stable at −34 mV. The above process involves mass transfer of Li ions through electrolyte, Li ion−solvent dissociation, reduction of Li ions, and the following electrocrystallization of formed Li atoms. From the above curve, the overpotential for the metallic Li deposition in the cell with EAA75 separator (Cu|EAA75|Li) is 20 mV. This value is lower than that with PE separator (28 mV) (Cu|PE|Li), indicating controllable nucleation kinetics for Li deposition in the Cu||Li cell. Meanwhile, fresh and uniform Li deposition is observed on the Cu foil with EAA75 separator. However, some dark dots are present with the PE separator (Figure S10), illuminating the inhomogeneous Li deposition. The Li plating onto Cu foil with pristine PE and EAA75 separators were further investigated by SEM. Figure S11 shows the top view SEM images of the morphologies for Li metal deposited on Cu foil at a current density of 0.5 mA cm^{-2}. Needle-like dendrites were distributed on the Cu electrode of Cu|PE|Li cell, while a flat Li deposition can be observed in Cu|EAA75|Li cell, confirming the dendrite inhibition effect of EAA75 because of the lower nucleation overpotential. These results are in accordance with literature that the introduction of poly(acrylic acid) (PAA) as electrolyte additive leads to stable Li plating/stripping.[42] In addition, Travas-Sejdic and co-workers have shown that the presence of PAA controls the Pt nanoparticle size and prevents aggregation during electrodeposition.[43]

The Li dendrite inhibition performance and cycling stability of the Li anode were further studied in Li||Li symmetric cells. Li|PE|Li and Li|EAA75|Li cells were assembled in the carbonate-based electrolyte (1 M $LiPF_6$ in EC/DEC = 1:1 vol/vol) with different current densities. As presented in Figure 4d, it could be operated stably approximately 380 h with PE at 0.5 mA cm^{-2} for 1.0 mAh cm^{-2}, and then the voltage increased suddenly, which means a short circuit happened in the cell. In contrast, the Li|EAA75|Li cell cycled over 1000 h without apparent voltage fluctuation, illustrating a uniform Li plating/stripping. Under a higher current density of 5 mA cm^{-2} (Figure 4e), the difference between PE and EAA75 is more noticeable. While the cell with PE could be barely operated and short circuit quickly, the cell with EAA75 shows extraordinary cycling stability for over 500 h with a voltage hysteresis of approximately 104 mV, illustrating a better cycling performance and dendrite inhibition at higher current densities with EAA75. Moreover, as displayed in Figure 4f,g, a dense and flat layer can be seen in the EAA75 based cells but many creaks are distributed on the Li anode with PE after cycling for 100 h at 0.5 mA cm^{-2}, indicating the formation of dendrites and electrolyte consumption. We demonstrate that EAA75 separators possess a unique ability to inhibit dendrite growth with the help of carboxyl groups. Improved cycling performance is attributed to the higher t_{Li^+} of EAA75 and more uniform pore size distribution, which allow for inhibition of dendrite growth and homogeneous lithium plating. Moreover, the faster anode kinetics of EAA75 facilitates the uniform formation of SEI. Collectively, features of the EAA75 separators provide improved battery safety and cycling stability.

EAA75 Separator for High-Energy-Density Batteries. The efficient suppression of Li dendrites enables highly improved battery rate capability. The commercial PE separator, which has the same backbone structure as EAA, was chosen to compare the electrochemical performance. As shown in Figure 5a,b, when assembled in $LiFePO_4$||Li (LFP||Li) cells, the discharge capacities of EAA75 separator are 151, 144, 132, 121, 109, and 98 mAh g^{-1} at 0.5, 1, 2, 3, 4, and 5 C, respectively. Compared with the PE separator, the EAA75 separator retains higher capacities at all rates, especially at high current density. The above results suggest that the EAA75 separators possess sufficient porosity for fast ion transport kinetics. Figure 5c displays the cycling performance of the LFP|EAA75|Li and LFP|PE|Li at 5 C. The initial capacity of EAA75 separator is

https://doi.org/10.1021/acsami.3c01311
ACS Appl. Mater. Interfaces 2023, 15, 18333−18342

107.0 mAh g^{-1}, while that of PE separator is 83.3 mAh g^{-1}. Meanwhile, the capacity decay of EAA75 separator (31%) is much lower than that of PE (54%) after 200 cycles, displaying the superior cycling performance of EAA75 separator at a 5 C high rate. Furthermore, the Coulombic efficiency of PE assembled battery fluctuated violently from the enlarged image (Figure S12), and it appeared over 100% frequently, which may cause temperature rising within the battery. The cells assembling EAA75 and PE were disassembled after cycling 200 circles at 5 C. As shown in Figure S13, the lithium anode of EAA75 is smoother than that of PE, illustrating the ability of EAA inhibiting lithium dendrites' growth. Higher t_{Li^+} and homogeneous SEI of EAA75 separator account for the stable cell cycling at high rate, which extends Li dendrite nucleation time and redistribute the Li^+ flux for stable Li plating/stripping. Additionally, the morphology of EAA75 after cycling was also characterized in Figure S14, illustrating the dimensional stability of EAA75.

To better understand how EAA75 separators inhibit the dendrite growth, a simple but vivid scheme was proposed. As shown in Figure 6, for commercial PE separators, due to its

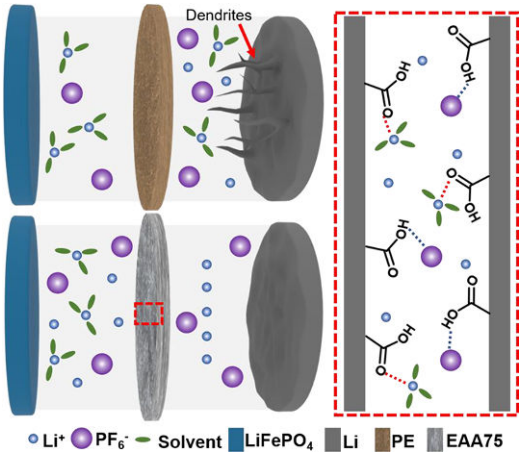


Figure 6. Schematic illustration of the Li deposition behaviors of LFP|PE|Li and LFP|EAA75|Li cell.

nonpolar backbone, both Li^+ and PF_6^- could simultaneously transfer, but PF_6^- exhibits higher mobility compared with Li^+, resulting in a lower t_{Li^+}.[44] Therefore, concentration polarization subsequently occur under an applied electric field, resulting in uneven lithium deposition, especially at high rates.[45,46] For EAA75, the carboxyl groups are helpful to the desolvation of Li^+ and the increase of Li^+ mobility, accounting for its superior ion conductivity. Meanwhile, hydrogen bonding between PF_6^- and carboxyl groups could inhibit PF_6^- crossing, leading to a high t_{Li^+} and efficiently suppressing dendrite growth. Moreover, the uniform and proper pore size of EAA75 separator facilitates the transport of Li^+ and redistribution of Li^+ flux. The synergistic effect of the above factors leads to efficient inhibition of lithium dendrites.

CONCLUSIONS

A novel nanoporous EAA75 separator with high dimensional stability was fabricated through a simple template-leaching method for LMBs, with a t_{Li^+} of up to 0.67. Solid state NMR and molecular dynamics simulations elucidated this increase, attributing it to immobilization of PF_6^- anions and accelerated transport of Li^+ cations along the carboxyl groups distributed on the pore surface. The EAA75 separator also demonstrated stability during Li plating/stripping cycling by accelerating the charge-transfer kinetics. Consequently, a long-term Li plating/stripping cycle lifetime of 500 h was achieved at a high current density of 5 mA cm^{-2}. The EAA75 separator could improve the rate capacity remarkably and deliver a discharge capacity of 107 mAh g^{-1} at 5 C without dendrite formation after 200 cycles. The results presented here provide a promising new material for separators with potential for practical applications in lithium batteries.

EXPERIMENTAL SECTION

Ethylene acrylic acid 6100 (EAA 6100) was purchased from SK Chemistry, with acrylic acid content of 10 wt %. Polyethylene glycol (PEG) 2000 and tetrahydrofuran (THF) was purchased from Sinopharm Chemical Reagent Co. (Shanghai, China). The liquid electrolyte (1 mol L^{-1} $LiPF_6$) in a mixed solvent of ethylene carbonate (EC) and diethyl carbonate (DEC) with volume ratio of 1:1 was purchased from Saibo Electrochemical Materials Network. Polyethylene (PE) was obtained from Jiangsheng Material Co. (Hubei, China).

Fabrication of EAA Separators. 0.7 g of EAA and various amounts of PEG 2000 (0.1, 0.3, 0.5, and 0.7 g) were dissolved in 10 mL of THF with magnetic stirring at 65 °C. After stirring for 1 h, the obtained solution was cast onto the glass substrate with a doctor blade of 750 μm at 60 °C. After standing for 1 min, the substrate was immersed into water to remove the THF and PEG 2000. The obtained EAA separator was transferred into ethanol and then dried at room temperature.

Characterization. The microstructure of the EAA separators were characterized by scanning electron microscopy (SEM, Hitachi S-4700). The contact angle was evaluated to compare the wetting properties of the separators toward liquid electrolyte by using a contact angle tester (OCA20). A capillary flow porometer (CFP-1500AE) was employed to measure the pore diameter of separators.

The electrolyte uptake was evaluated by measuring the weight of the membranes before and after immersing into the liquid electrolyte (eq 4):

$$\text{uptake} = \frac{m_2 - m_1}{m_1} \times 100\% \tag{4}$$

where m_1 and m_2 were the weight of the separator before and after being immersed in the liquid electrolyte.

The porosity was obtained through measuring the weight of membrane before and after immersing into *n*-butanol (eq 5):

$$\text{porosity} = \frac{m_4 - m_3}{V \times \rho} \times 100\% \tag{5}$$

where m_3 and m_4 were the weight of separators before and after immersed into *n*-butanol, V was the volume of separators, and ρ was the density of *n*-butanol (ρ = 0.81 g cm^{-3}).

Electrochemical Measurements. Ionic conductivity was evaluated by the electrochemical spectra (EIS) using Autolab (PGSTAT 302N), which can be calculated via eq 6:

$$\sigma = \frac{d}{R_d \times S} \tag{6}$$

where d, R_d, and S are the thickness of the separator, bulk resistance, the area of the electrode, respectively.

The electrochemical stability was measured from liner sweep voltammetry (LSV) from 2.5 to 5.0 V at a scan rate of 1 mV s^{-1}.

Lithium ion transference number (t_{Li^+}) was evaluated by combining chronoamperometry and EIS analysis using Li symmetric cells. t_{Li^+} was calculated according to eq 7:

$$t_{Li^+} = \frac{I_s(\Delta V - I_0 R_0)}{I_0(\Delta V - I_s R_s)} \tag{7}$$

https://doi.org/10.1021/acsami.3c01311
ACS Appl. Mater. Interfaces 2023, 15, 18333−18342

where I_0 and I_s are the initial current and steady-state current (where the plot is flat), R_0 and R_s are the interfacial resistance before and after polarization, respectively, and ΔV is the potential difference (10 mV).

The battery performance of separators was examined by using the $LiFePO_4$/separator-liquid electrolyte/lithium coin-type cell, which was assembled in a glovebox. The testing voltage was 2.5−3.9 V.

The Li||Li symmetric cells and Cu||Li cells were assembled with different separators.

The Tafel plot was obtained from cyclic voltammetry (CV) curves with a scan rate of 1 mV s^{-1}, and the exchange current density was calculated from the Tafel plot through Bulter−Vlomer equation.

Molecular Dynamics Simulations. Classical molecular dynamics simulations were carried out to model the experimental systems. The ethylene and acrylic acid monomers, diethyl carbonate and Li^+ were parametrized by the CHARMM36 force field, while ethylene carbonate and PF_6^- were parametrized with CGenFF and Gaussian, respectively. The systems were simulated in an NpT ensemble (T = 300 K, p = 1 bar) using a Langevin dynamics (γ_{lang} = 1 ps^{-1}) in NAMD 2.13. The particle-mesh Ewald (PME) method was used to evaluate the long-range Coulomb interaction. The hydrogen bonding and long-range Coulombic interaction were evaluated every 1 and 2 timesteps (time step of 1 fs), respectively. After 10,000 steps of minimization, the systems were simulated in an electric field of E = 1.3 MV/m. Velocities and current measurements were extracted from the final trajectories.

■ ASSOCIATED CONTENT

Supporting Information

The Supporting Information is available free of charge at https://pubs.acs.org/doi/10.1021/acsami.3c01311.

> Porosity and average pore size of PE and EAA separators; cross-sectional SEM images of EAA75 separators; contact angels of PE and EAA75 separators; Nyquist plot of PE and EAA75; EIS spectra of PE and EAA75; photographs and SEM images of Cu electrodes disassembling from Cu|PE|Li and Cu|EAA75|Li after Li plating; Coulombic efficiency of PE and EAA75 assembled batteries (PDF)

■ AUTHOR INFORMATION

Corresponding Authors

Hui Nie − *Key Laboratory of Material Chemistry for Energy Conversion and Storage, Ministry of Education, School of Chemistry and Chemical Engineering, Huazhong University of Science and Technology, Wuhan 430074, China;* orcid.org/0000-0001-7422-4910; Email: huinie@hust.edu.cn

Petr Kral − *Department of Chemistry and Departments of Physics, Pharmaceutical Sciences, and Chemical Engineering, University of Illinois at Chicago, Chicago, Illinois 60607, United States;* orcid.org/0000-0003-2992-9027; Email: pkral@uic.edu

Xiaolin Xie − *Key Laboratory of Material Chemistry for Energy Conversion and Storage, Ministry of Education, School of Chemistry and Chemical Engineering, Huazhong University of Science and Technology, Wuhan 430074, China;* orcid.org/0000-0001-5097-7416; Email: xlxie@hust.edu.cn

Authors

Yi Chen − *Key Laboratory of Material Chemistry for Energy Conversion and Storage, Ministry of Education, School of Chemistry and Chemical Engineering, Huazhong University of Science and Technology, Wuhan 430074, China*

Philip Mickel − *Department of Chemistry, University of Illinois at Chicago, Chicago, Illinois 60607, United States*

Huijie Pei − *Key Laboratory of Material Chemistry for Energy Conversion and Storage, Ministry of Education, School of Chemistry and Chemical Engineering, Huazhong University of Science and Technology, Wuhan 430074, China*

Yingfeng Wen − *Key Laboratory of Material Chemistry for Energy Conversion and Storage, Ministry of Education, School of Chemistry and Chemical Engineering, Huazhong University of Science and Technology, Wuhan 430074, China*

Xin Guan − *Key Laboratory of Material Chemistry for Energy Conversion and Storage, Ministry of Education, School of Chemistry and Chemical Engineering, Huazhong University of Science and Technology, Wuhan 430074, China*

Yun Wang − *Key Laboratory of Material Chemistry for Energy Conversion and Storage, Ministry of Education, School of Chemistry and Chemical Engineering, Huazhong University of Science and Technology, Wuhan 430074, China*

Xuyang Wang − *Key Laboratory of Material Chemistry for Energy Conversion and Storage, Ministry of Education, School of Chemistry and Chemical Engineering, Huazhong University of Science and Technology, Wuhan 430074, China*

Omar Al Mhtachem − *Department of Chemistry, University of Illinois at Chicago, Chicago, Illinois 60607, United States*

Cheng Zhang − *Australian Institute for Bioengineering and Nanotechnology and ARC Centre of Excellence in Convergent Bio-Nano Science and Technology, The University of Queensland, Brisbane, Queensland 4072, Australia;* orcid.org/0000-0002-2722-7497

Xingping Zhou − *Key Laboratory of Material Chemistry for Energy Conversion and Storage, Ministry of Education, School of Chemistry and Chemical Engineering, Huazhong University of Science and Technology, Wuhan 430074, China;* orcid.org/0000-0001-9886-7961

Complete contact information is available at: https://pubs.acs.org/10.1021/acsami.3c01311

Notes

The authors declare no competing financial interest.

■ ACKNOWLEDGMENTS

The authors acknowledge financial supports from Major International (Regional) Joint Cooperation Research Project of National Natural Science Foundation of China (52020105012), the Fundamental Research Funds for the Central Universities (2022JYCXJJ054), the Innovation and Talent Recruitment Base of New Energy Chemistry and Device (B21003) and analytical and testing assistance from the Analysis and Testing Center of HUST. C.Z. acknowledges support from the National Health and Medical Research Council for the CJ Martin Fellowship (APP1157440) and the Australian Research Council Discovery Early Career Researcher Awards (DECRA) Fellowship (DE230101105).

■ REFERENCES

(1) Yuan, M.; Liu, K. Rational Design on Separators and Liquid Electrolytes for Safer Lithium-Ion Batteries. *J. Energy Chem.* **2020**, *43*, 58−70.

(2) Lau, J.; DeBlock, R. H.; Butts, D. M.; Ashby, D. S.; Choi, C. S.; Dunn, B. S. Sulfide Solid Electrolytes for Lithium Battery Applications. *Adv. Energy Mater.* **2018**, *8* (27), 1800933.

(3) Liang, S.; Cheng, Y. J.; Zhu, J.; Xia, Y.; Müller-Buschbaum, P. A Chronicle Review of Nonsilicon (Sn, Sb, Ge)-Based Lithium/Sodium-Ion Battery Alloying Anodes. *Small Methods* **2020**, *4* (8), 2000218.
(4) Lee, H.; Yanilmaz, M.; Toprakci, O.; Fu, K.; Zhang, X. A Review of Recent Developments in Membrane Separators for Rechargeable Lithium-Ion Batteries. *Energy Environ. Sci.* **2014**, *7* (12), 3857−3886.
(5) Yuan, B.; Wen, K.; Chen, D.; Liu, Y.; Dong, Y.; Feng, C.; Han, Y.; Han, J.; Zhang, Y.; Xia, C.; et al. Composite Separators for Robust High Rate Lithium Ion Batteries. *Adv. Funct. Mater.* **2021**, *31* (32), 2101420.
(6) Wang, J.; Liu, Y.; Cai, Q.; Dong, A.; Yang, D.; Zhao, D. Hierarchically Porous Silica Membrane as Separator for High-Performance Lithium-Ion Batteries. *Adv. Mater.* **2022**, *34* (3), 2107957.
(7) Zhang, Y.; Qiu, Z.; Wang, Z.; Yuan, S. Functional Polyethylene Separator with Impurity Entrapment and Faster Li^+ Ions Transfer for Superior Lithium-Ion Batteries. *J. Colloid Interface Sci.* **2022**, *607*, 742−751.
(8) Liu, B.; Zhang, J.-G.; Xu, W. Advancing Lithium Metal Batteries. *Joule* **2018**, *2* (5), 833−845.
(9) Li, C.; Qin, B.; Zhang, Y.; Varzi, A.; Passerini, S.; Wang, J.; Dong, J.; Zeng, D.; Liu, Z.; Cheng, H. Single-Ion Conducting Electrolyte Based on Electrospun Nanofibers for High-Performance Lithium Batteries. *Adv. Energy Mater.* **2019**, *9* (10), 1803422.
(10) Ma, L.; Fu, C.; Li, L.; Mayilvahanan, K. S.; Watkins, T.; Perdue, B. R.; Zavadil, K. R.; Helms, B. A. Nanoporous Polymer Films with a High Cation Transference Number Stabilize Lithium Metal Anodes in Light-Weight Batteries for Electrified Transportation. *Nano Lett.* **2019**, *19* (2), 1387−1394.
(11) Zhao, Q.; Zhou, R.; Wang, C.; Kang, J.; Zhang, Q.; Liu, J.; Jin, Y.; Wang, H.; Zheng, Z.; Guo, L. Anion Immobilization Enabled by Cation-Selective Separators for Dendrite-Free Lithium Metal Batteries. *Adv. Funct. Mater.* **2022**, *32* (23), 2112711.
(12) Sand, H. J. S. III. On the Concentration at the Electrodes in a Solution, with Special Reference to the Liberation of Hydrogen by Electrolysis of a Mixture of Copper Sulphate and Sulphuric Acid. *Philos. Mag.* **1901**, *1* (1), 45−79.
(13) Li, L.; Wang, M.; Wang, J.; Ye, F.; Wang, S.; Xu, Y.; Liu, J.; Xu, G.; Zhang, Y.; Zhang, Y.; et al. Asymmetric Gel Polymer Electrolyte with High Lithium Ion Conductivity for Dendrite-Free Lithium Metal Batteries. *J. Mater. Chem. A* **2020**, *8* (16), 8033−8040.
(14) Kim, D.; Liu, X.; Yu, B.; Mateti, S.; O'Dell, L. A.; Rong, Q.; Chen, Y. Amine-Functionalized Boron Nitride Nanosheets: A New Functional Additive for Robust, Flexible Ion Gel Electrolyte with High Lithium-Ion Transference Number. *Adv. Funct. Mater.* **2020**, *30* (15), 1910813.
(15) Huo, H.; Li, X.; Chen, Y.; Liang, J.; Deng, S.; Gao, X.; Doyle-Davis, K.; Li, R.; Guo, X.; Shen, Y.; et al. Bifunctional Composite Separator with a Solid-State-Battery Strategy for Dendrite-Free Lithium Metal Batteries. *Energy Storage Mater.* **2020**, *29*, 361−366.
(16) Lee, H.; Ren, X.; Niu, C.; Yu, L.; Engelhard, M. H.; Cho, I.; Ryou, M. H.; Jin, H. S.; Kim, H. T.; Liu, J.; et al. Suppressing Lithium Dendrite Growth by Metallic Coating on a Separator. *Adv. Funct. Mater.* **2017**, *27* (45), 1704391.
(17) Liu, Y.; Tao, X.; Wang, Y.; Jiang, C.; Ma, C.; Sheng, O.; Lu, G.; Lou, X. W. Self-Assembled Monolayers Direct a LiF-Rich Interphase toward Long-Life Lithium Metal Batteries. *Science* **2022**, *375*, 739−745.
(18) Kim, P. J.; Pol, V. G. High Performance Lithium Metal Batteries Enabled by Surface Tailoring of Polypropylene Separator with a Polydopamine/Graphene Layer. *Adv. Energy Mater.* **2018**, *8* (36), 1802665.
(19) Choi, i.-H.; Kang, H.-J.; Ryu, E.-N.; Lee, K.-P. Electrochemical Properties of Polyolefin Nonwoven Fabric Modified with Carboxylic Acid Group for Battery Separator. *Radiat. Phys. Chem.* **2001**, *60* (4), 495−502.
(20) Song, Q.; Li, A.; Shi, L.; Qian, C.; Feric, T. G.; Fu, Y.; Zhang, H.; Li, Z.; Wang, P.; Li, Z.; et al. Thermally Stable, Nano-Porous and Eco-Friendly Sodium Alginate/Attapulgite Separator for Lithium-Ion Batteries. *Energy Storage Mater.* **2019**, *22*, 48−56.
(21) Yang, Y.; Wang, W.; Meng, G.; Zhang, J. Function-directed Design of Battery Separators Based on Microporous Polyolefin Membranes. *J. Mater. Chem. A* **2022**, *10* (27), 14137−14170.
(22) Zhang, M.; Guan, K.; Ji, Y.; Liu, G.; Jin, W.; Xu, N. Controllable Ion Transport by Surface-Charged Graphene Oxide Membrane. *Nat. Commun.* **2019**, *10* (1), 1253.
(23) Shen, L.; Wu, H. B.; Liu, F.; Brosmer, J. L.; Shen, G.; Wang, X.; Zink, J. I.; Xiao, Q.; Cai, M.; Wang, G.; et al. Creating Lithium-Ion Electrolytes with Biomimetic Ionic Channels in Metal-Organic Frameworks. *Adv. Mater.* **2018**, *30* (23), 1707476.
(24) Shi, W.; Shen, J.; Shen, L.; Hu, W.; Xu, P.; Baucom, J. A.; Ma, S.; Yang, S.; Chen, X. M.; Lu, Y. Electrolyte Membranes with Biomimetic Lithium-Ion Channels. *Nano Lett.* **2020**, *20* (7), 5435−5442.
(25) Parekh, M. H.; Oka, S.; Lutkenhaus, J.; Pol, V. G. Critical-Point-Dried, Porous, and Safer Aramid Nanofiber Separator for High-Performance Durable Lithium-Ion Batteries. *ACS Appl. Mater. Interfaces* **2022**, *14* (25), 29176−29187.
(26) Toivonen, M. S.; Onelli, O. D.; Jacucci, G.; Lovikka, V.; Rojas, O. J.; Ikkala, O.; Vignolini, S. Anomalous-Diffusion-Assisted Brightness in White Cellulose Nanofibril Membranes. *Adv. Mater.* **2018**, *30* (16), 1704050.
(27) Zhang, K.; Liu, W.; Gao, Y.; Wang, X.; Chen, Z.; Ning, R.; Yu, W.; Li, R.; Li, L.; Li, X.; et al. A High-Performance Lithium Metal Battery with Ion-Selective Nanofluidic Transport in a Conjugated Microporous Polymer Protective Layer. *Adv. Mater.* **2021**, *33* (5), 2006323.
(28) Lin, C.-E.; Zhang, H.; Song, Y.-Z.; Zhang, Y.; Yuan, J.-J.; Zhu, B.-K. Carboxylated Polyimide Separator with Excellent Lithium Ion Transport Properties for a High-Power Density Lithium-ion Battery. *J. Mater. Chem. A* **2018**, *6* (3), 991−998.
(29) Wang, Y.; Deng, Z.; Luo, B.; Duan, G.; Zheng, S.; Sun, L.; Ye, Z.; Lu, J.; Huang, J.; Lu, Y. Highly Reversible Zn Metal Anodes Realized by Synergistically Enhancing Ion Migration Kinetics and Regulating Surface Energy. *Adv. Funct. Mater.* **2022**, *32* (52), 2209028.
(30) Kumar, N.; Seminario, J. M. Lithium-Ion Model Behavior in an Ethylene Carbonate Electrolyte Using Molecular Dynamics. *J. Phys. Chem. C* **2016**, *120* (30), 16322−16332.
(31) Ong, M. T.; Verners, O.; Draeger, E. W.; van Duin, A. C.; Lordi, V.; Pask, J. E. Lithium Ion Solvation and Diffusion in Bulk Organic Electrolytes from First-principles and Classical Reactive Molecular Dynamics. *J. Phys. Chem. B* **2015**, *119* (4), 1535−1545.
(32) Kral, P.; Wang, B. Material Drag Phenomena in Nanotubes. *Chem. Rev.* **2013**, *113* (5), 3372−3390.
(33) Vukovic, L.; Vokac, E.; Kral, P. Molecular Friction-Induced Electroosmotic Phenomena in Thin Neutral Nanotubes. *J. Phys. Chem. Lett.* **2014**, *5* (12), 2131−2137.
(34) Zhao, Q.; Wang, R.; Hu, X.; Wang, Y.; Lu, G.; Yang, Z.; Liu, Q.; Yang, X.; Pan, F.; Xu, C. Functionalized 12 μm Polyethylene Separator to Realize Dendrite-Free Lithium Deposition toward Highly Stable Lithium-Metal Batteries. *Adv. Sci.* **2022**, *9* (13), 2102215.
(35) Ma, Y.; Wei, L.; He, Y.; Yuan, X.; Su, Y.; Gu, Y.; Li, X.; Zhao, X.; Qin, Y.; Mu, Q.; et al. A "Blockchain" Synergy in Conductive Polymer-Filled Metal-Organic Frameworks for Dendrite-Free Li Plating/Stripping with High Coulombic Efficiency. *Angew. Chem., Int. Ed.* **2022**, *61* (12), 202116291.
(36) Li, S.; Wang, X. S.; Han, B.; Lai, C.; Shi, P. R.; Ma, J. B.; Wang, S. W.; Zhang, L. H.; Liu, Q.; Deng, Y. H.; et al. Ultrathin and High-Modulus $LiBO_2$ Layer Highly Elevates the Interfacial Dynamics and Stability of Lithium Anode under Wide Temperature Range. *Small* **2022**, *18* (8), 2106427.
(37) You, J.; Deng, H.; Zheng, X.; Yan, H.; Deng, L.; Zhou, Y.; Li, J.; Chen, M.; Wu, Q.; Zhang, P.; et al. Stabilized and Almost Dendrite-Free Li Metal Anodes by In Situ Construction of a Composite Protective Layer for Li Metal Batteries. *ACS Appl. Mater. Interfaces* **2022**, *14* (4), 5298−5307.

https://doi.org/10.1021/acsami.3c01311
ACS Appl. Mater. Interfaces 2023, 15, 18333−18342

(38) Bard, A. J.; Faulkner, L. R.; White, H. S. *Electrochemical Methods: Fundamentals and Applications*; Wiley, 2022; p 102.
(39) Morey, M.; Loftus, J.; Cannon, A.; Ryan, E. Interfacial Studies on the Effects of Patterned Anodes for Guided Lithium Deposition in Lithium Metal Batteries. *J. Chem. Phys.* **2022**, *156* (1), 014703.
(40) Chen, X.; Zhang, R.; Zhao, R.; Qi, X.; Li, K.; Sun, Q.; Ma, M.; Qie, L.; Huang, Y. A "Dendrite-eating" Separator for High-Areal-Capacity Lithium-Metal Batteries. *Energy Storage Mater.* **2020**, *31*, 181−186.
(41) Ghazi, Z. A.; Sun, Z.; Sun, C.; Qi, F.; An, B.; Li, F.; Cheng, H. M. Key Aspects of Lithium Metal Anodes for Lithium Metal Batteries. *Small* **2019**, *15* (32), 1900687.
(42) Xue, C.; Zhang, X.; Wang, S.; Li, L.; Nan, C. W. Organic-Organic Composite Electrolyte Enables Ultralong Cycle Life in Solid-State Lithium Metal Batteries. *ACS Appl. Mater. Interfaces* **2020**, *12* (22), 24837−24844.
(43) Hackett, A. J.; Malmström, J.; Travas-Sejdic, J. Grafting Poly(acrylic acid) from PEDOT To Control the Deposition and Growth of Platinum Nanoparticles for Enhanced Electrocatalytic Hydrogen Evolution. *ACS Appl. Energy Mater.* **2019**, *2* (2), 1436−1444.
(44) Zhang, C.; Shen, L.; Shen, J.; Liu, F.; Chen, G.; Tao, R.; Ma, S.; Peng, Y.; Lu, Y. Anion-Sorbent Composite Separators for High-Rate Lithium-Ion Batteries. *Adv. Mater.* **2019**, *31* (21), 1808338.
(45) Zhou, M.; Liu, R.; Jia, D.; Cui, Y.; Liu, Q.; Liu, S.; Wu, D. Ultrathin Yet Robust Single Lithium-Ion Conducting Quasi-Solid-State Polymer-Brush Electrolytes Enable Ultralong-Life and Dendrite-Free Lithium-Metal Batteries. *Adv. Mater.* **2021**, *33* (29), 2100943.
(46) Li, G.; Liu, Z.; Wang, D.; He, X.; Liu, S.; Gao, Y.; AlZahrani, A.; Kim, S. H.; Chen, L.-Q.; Wang, D. Electrokinetic Phenomena Enhanced Lithium-Ion Transport in Leaky Film for Stable Lithium Metal Anodes. *Adv. Energy Mater.* **2019**, *9* (22), 1900704.

Recommended by ACS

Diviologen-Functionalized Poly(arylene ether ketone)s with Improved Stability and Rate Performance for Polymer Batteries
Jiaqi Xu, Dongyang Chen, *et al.*
APRIL 05, 2023
ACS APPLIED ENERGY MATERIALS
READ

Autonomous Healable Elastomers with High Elongation, Stiffness, and Fatigue Resistance
Jiacheng Ma and Shifeng Wen
MARCH 23, 2023
LANGMUIR
READ

Unraveling the Interphasial Chemistry for Highly Reversible Aqueous Zn Ion Batteries
Xuesong Zhao, Huilin Pan, *et al.*
JANUARY 17, 2023
ACS APPLIED MATERIALS & INTERFACES
READ

Li^+ Conduction in Glass-Forming Single-Ion Conducting Polymer Electrolytes with and without Ion Clusters
Jiacheng Liu and Jennifer L. Schaefer
MARCH 16, 2023
MACROMOLECULES
READ

Get More Suggestions >

https://doi.org/10.1021/acsami.3c01311
ACS Appl. Mater. Interfaces 2023, 15, 18333−18342